STRUCTURAL BIOLOGY

Unveiling the structural mechanisms of nonpeptide ligand recognition and activation in human chemokine receptor CCR8

Shan Jiang[1,2]†, Xi Lin[1]†, Lijie Wu[1]†, Ling Wang[1], Yiran Wu[1], Ziyi Xu[1,2], Fei Xu[1,2,3]*

The human CC chemokine receptor 8 (CCR8) is an emerging therapeutic target for cancer immunotherapy and autoimmune diseases. Understanding the molecular recognition of CCR8, particularly with nonpeptide ligands, is valuable for drug development. Here, we report three cryo–electron microscopy structures of human CCR8 complexed with G_i trimers in the ligand-free state or activated by nonpeptide agonists LMD-009 and ZK 756326. A conserved $Y^{1.39}Y^{3.32}E^{7.39}$ motif in the orthosteric binding pocket is shown to play a crucial role in the chemokine and nonpeptide ligand recognition. Structural and functional analyses indicate that the lack of conservation in $Y114^{3.33}$ and $Y172^{4.64}$ among the CC chemokine receptors could potentially contribute to the selectivity of the nonpeptide ligand binding to CCR8. These findings present the characterization of the molecular interaction between a nonpeptide agonist and a chemokine receptor, aiding the development of therapeutics targeting related diseases through a structure-based approach.

INTRODUCTION

Chemokine receptors (CKRs) are G protein–coupled receptors (GPCRs) activated by small protein ligands called chemokines (*1*). Chemokines interact with CKRs and have a wide range of functions in immune defense (*2*–*4*). Therefore, they are involved in a range of diseases, including inflammation, cancer, and autoimmune disorders (*5*). Currently, more than 50 endogenous chemokines and 20 CKRs have been identified in human (*6*). The diversity and promiscuity of chemokine system result in biased signaling and functional selectivity (*7*). Recently, several CKRs with G protein complex structures have been resolved in the absence of exogenous ligand stimulation, including CC chemokine receptor 1 (CCR1)–G_i (*8*), CCR3-G_i (*9*), and CCR5-G_i (*10*), revealing their constitutive activation of downstream signaling pathways (*11*). Despite remarkable progress in structural studies of CKR–G protein complexes in recent years, a comprehensive understanding of the conserved molecular mechanism underlying constitutive activity within the CKR family, as well as the mechanism by which a nonpeptide agonist recognizes the receptor to activate downstream signaling, remains elusive.

CC CCR8 shows great potential as a drug target for cancer immunotherapy and autoimmune disorders. Tumor-infiltrating regulatory T cells (T_{regs}) that inhibit the antitumor effector T cell responses were found to have highly enriched and specifically expressed CCR8 (*12*). CCR8 is the only known receptor for CCL1 (*13*), and the binding of CCL1 to CCR8 on human T_{regs} is crucial for its inhibitory activity (*14*). Blocking the CCL1-CCR8 axis through anti-CCL1 or anti-CCR8 antibodies may enhance antitumor immune responses and reduce tumor burden (*15*). Some antibodies targeting CCR8 have been used in clinical trials to treat solid tumors, such as BSM-986340 (*16*) and LM-108 (*17*). Conversely, in an experimental model for multiple sclerosis (experimental autoimmune encephalomyelitis), the CCL1-Ig fusion protein inhibits disease progression by activating CCR8 in T_{reg} cells (*18*). All these findings indicate that CCR8 plays complex roles for various diseases, with potential applications for both receptor agonists and antagonists (*19*).

Compared with antibody drugs, small molecules can act on targets with clear mechanism and desired route of administration. However, the underlying mechanism for selectivity of small-molecule drugs and their way to activate downstream signaling is poorly understood. Here, we resolved three atomic-resolution structures of the G_i protein–coupled human CCR8 using single-particle cryo–electron microscopy (cryo-EM) method, including apo-CCR8-G_i, LMD-009–CCR8–G_i, and ZK 756326–CCR8–G_i [LMD-009 (*20*) and ZK 756326 (*21*) are CCR8 nonpeptide agonist]. The ligand-free and G_i-coupled CCR8 exhibits a substantial constitutive activity of CCR8, which is consistent with the functional characterization. Two agonist-bound CCR8 structures present features of the orthosteric ligand-binding pocket for nonpeptide ligand recognition. Furthermore, structural comparison with other solved CC CKRs uncovered the conserved mechanism/motif of CC CKR activation. Together, our analysis should provide an integrated understanding of the structure and function of CCR8, which paves the way to structure-based drug discovery for CKRs.

RESULTS

Structural determination of CCR8-G_i complexes

It is known that some CKRs, including CCR2 and CCR5, can activate downstream signaling without ligand stimulation (*22*). Several structures of CKRs in complex with G proteins in the absence of exogenous ligand stimulation have been reported recently (*8*–*10*). There is increasing evidence supporting that CCR8 can activate downstream G_i signaling (*19*). To investigate whether CCR8 has a high level of constitutive activity through G_i pathway, we performed bioluminescence resonance energy transfer (BRET) assays (*23*) to measure G protein heterotrimer dissociation in the absence of a ligand (*24*). The results revealed that CCR8 displayed high constitutive activity, as evidenced by a notable decrease in its BRET signal compared

[1]iHuman Institute, ShanghaiTech University, Pudong, Shanghai 201210, China. [2]School of Life Science and Technology, ShanghaiTech University, Shanghai 201210, China. [3]Shanghai Clinical Research Center, Shanghai 201210, China.
*Corresponding author. Email: xufei@shanghaitech.edu.cn
†These authors contributed equally to this work.

to negative controls of empty vector (mock control) and adenosine A_{2A} receptor [$A_{2A}R$; known to not couple to G_i (*25*)] as well as positive control GPR20 [known to self-activate G_i signaling (*26*)] (fig. S1A). Consistent with the functional assay that CCR8 exhibits high constitutive activity, we were able to obtain a stable CCR8-G_i complex in the absence of an agonist and resolve the structure through cryo-EM (see Materials and Methods and fig. S1). The complex was composed of the wild-type (WT) CCR8 with a C-terminal LgBiT fusion (*27*), dominant-negative mutant of $G_{\alpha i1}$ [containing three mutations: S47N, G203A, and A326S (*28*)], $G_{\beta 1}$ with a C-terminal HiBiT (*27*), WT $G_{\gamma 2}$, and the single-chain stabilizing antibody fragment scFv16 (*29*). All of these components could be clearly identified by two-dimensional (2D) classification, indicating the successful formation of the stable apo-CCR8-G_i complex for cryo-EM structural analysis (fig. S1C). The apo-CCR8-G_i complex displays typical features of GPCR–G protein, with no continuous extra density observed in the orthosteric pocket of CCR8 (fig. S2). Last, the structure of the ligand-free CCR8-G_i complex was determined at a global resolution of 3.31 Å (Fig. 1, fig. S1, and table S1).

At present, it has been generally accepted that chemokine binding to CKRs uses the classic "two-site" model (*8*), but the molecular mechanism underlying nonpeptide agonist recognition in CKRs remains unclear. Nonpeptide agonists are crucial for understanding the mechanism of receptor activation and designing effective nonpeptide ligands for CKRs. To investigate the molecular mechanisms of nonpeptide ligand recognition and activation in CCR8, we determined the cryo-EM structures of LMD-009–CCR8–G_i and ZK 756326–CCR8–G_i, with resolutions of 2.96 and 3.06 Å, respectively, (Fig. 1, figs. S3 and S4, and table S1).

The $Y^{1.39}Y^{3.32}E^{7.39}$ motif for ligand binding in CC CKRs

8-[[3-(2-Methoxyphenoxy)phenyl]methyl]-1-(2-phenethyl)-1,3,8-triazaspiro[4,5]decan-4-one (LMD-009) (*20*) and 2-[2-[4-[(3-phenoxyphenyl)methyl]piperazin-1-yl] ethoxy]ethanol (ZK 756326) (*21*) are nonpeptide agonists of CCR8, which exhibit a common feature of a centrally located positively charged amine, a characteristic shared by many nonpeptide antagonists of CKRs (Fig. 2, A and B) (*30*). In both LMD-009–CCR8–G_i and ZK 756326–CCR8–G_i complexes, CCR8 displays a ligand-binding pocket situated on the extracellular side of the transmembrane domain (TMD) (Fig. 2, A and B). LMD-009 and ZK 756326 bind to CCR8 in a similar position formed by TM1, TM2–4, and TM6–7. The interactions between CCR8 and ligands mainly involve hydrogen bonds and hydrophobic contacts (Fig. 2, C and E). The two ligands establish two sets of hydrogen bond interactions with CCR8: ZK 756326 interacting with $E286^{7.39}$ and $Y114^{3.33}$ (Fig. 2C), while LMD-009 with $E286^{7.39}$ and $Y172^{4.64}$ (Fig. 2E). LMD-009 and ZK 756326 are further stabilized in the pocket through contacts with a group of hydrophobic residues, including $Y42^{1.39}$, $V109^{3.28}$, $Y113^{3.32}$, and $F254^{6.51}$ (Fig. 2, C and E). Mutations of all these residues reduced the efficacy and affinity of the two ligands in activating CCR8, thereby validating our structural findings (Fig. 2, D and F, and table S2).

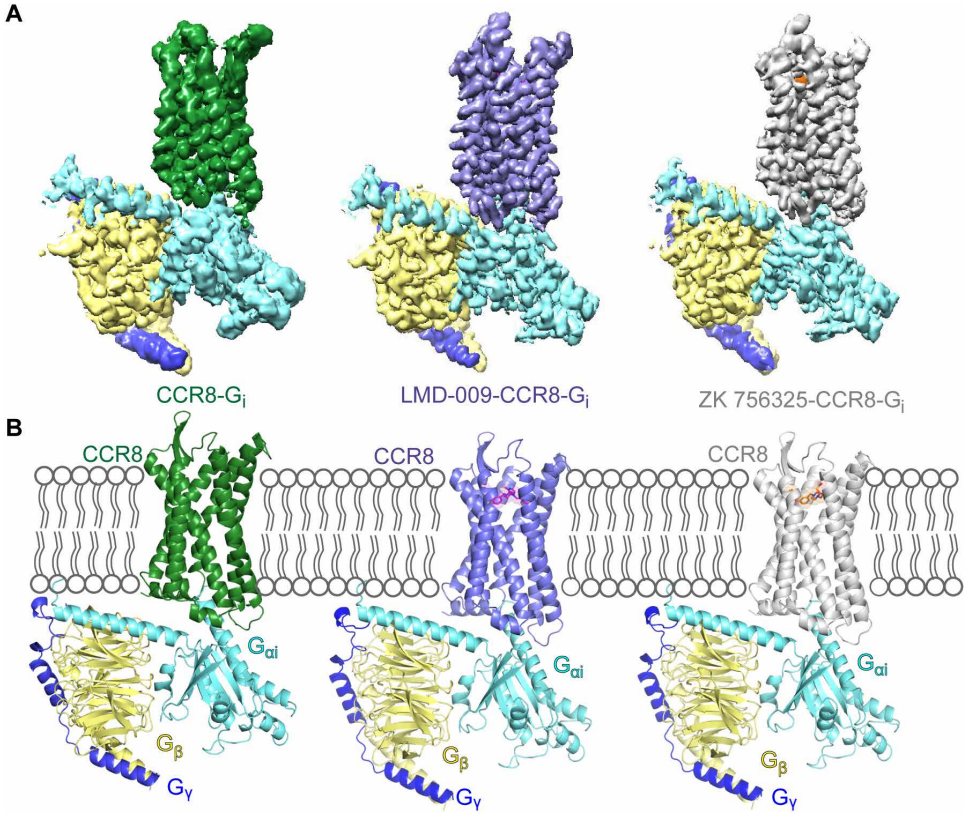

Fig. 1. Cryo-EM structures of the apo-CCR8-G_i, LMD-009–CCR8–G_i, and ZK 756326–CCR8–G_i complexes. (**A** and **B**) Cryo-EM map (A) and cartoon representation of the atomic model (B) of the apo-CCR8-G_i (left), LMD-009–CCR8–G_i (middle), and ZK 756326–CCR8–G_i (right) complexes were shown, respectively. Color coding is annotated for each protein component.

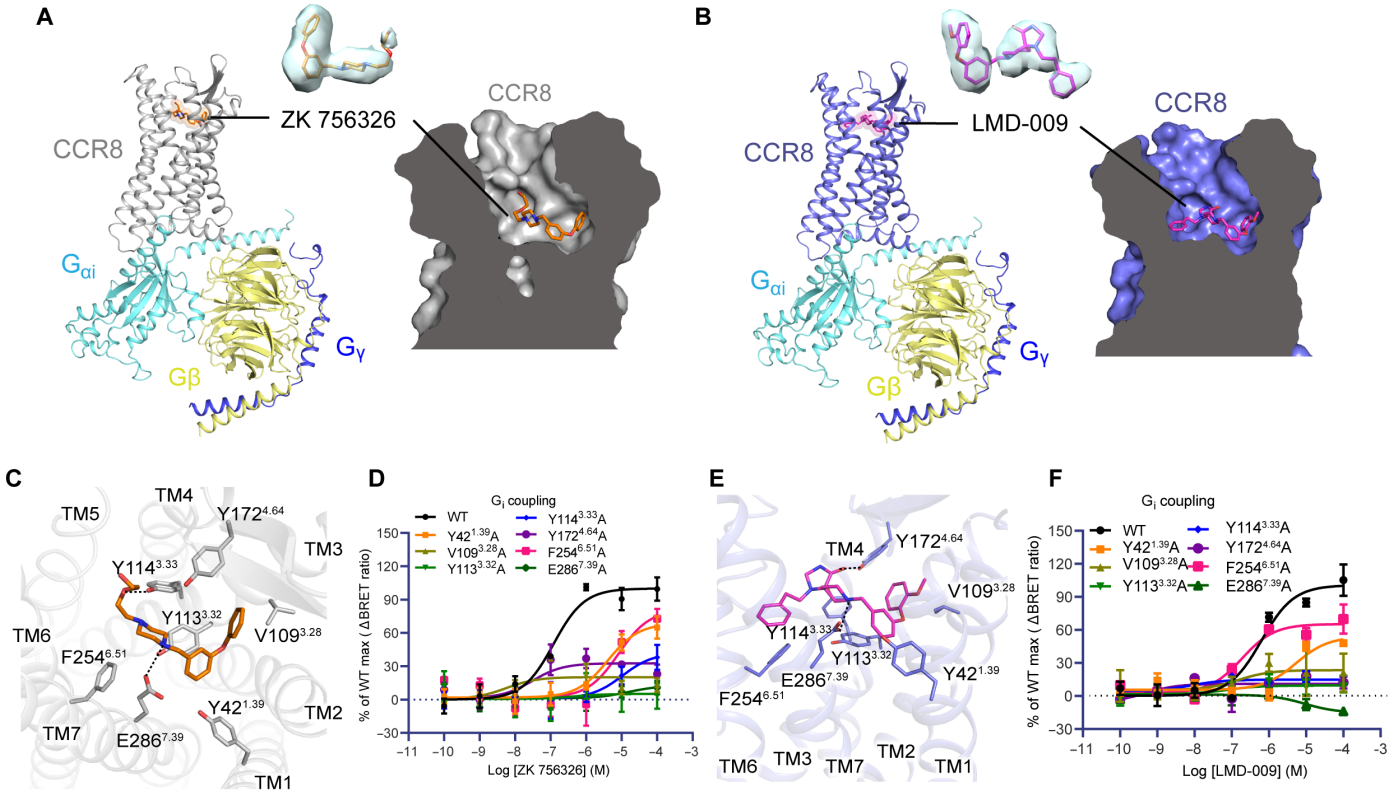

Fig. 2. The nonpeptide agonist binding pocket. (**A** and **B**) Overall structure of CCR8-G_i complex bound to ZK 756326 (A) or LMD-009 (B), with the orthosteric pocket zoomed in through a sectional view. (**C** and **E**) Key residues involved in ZK 756326 (C) or LMD-009 (E) binding in CCR8-G_i complex structures. The residues involved in interactions are shown as sticks, and hydrogen bonds are highlighted with black dashed lines. (**D** and **F**) Mutagenesis and functional measurement ($G_{\alpha\beta\gamma}$ heterotrimer dissociation by BRET assay) of ZK 756326 (D)– or LMD-009 (F)–induced G_i activation of CCR8. Data are shown as means ± SEM from at least three independent experiments performed in technical triplicates.

Notably, both ligands bind to a family conserved and functionally versatile residue $E286^{7.39}$, which forms diverse interactions in previously reported CKR structures. For example, in the CCR5-maraviroc complex (*31*) [Protein Data Bank (PDB): 4MBS], $E286^{7.39}$ forms a salt bridge with the ligand, while in the CCR2-RA[R]-BMS-618 (*32*) (PDB: 5T1A) complex, it does not engage direct interaction with the ligand (Fig. 3, E and F). Mutation of $E286^{7.39}$ to alanine abolished agonist-induced activation in CCR8 (Fig. 2, D and F).

Since most CKRs transmit signals through the G_i protein, we further compared the ligand-binding pocket of CCR8 with all reported structures of G_i-coupled CKRs, and found that there is a conserved motif $Y^{1.39}Y^{3.32}E^{7.39}$ in the orthosteric pocket, which seems essential for both chemokine and nonpeptide ligand recognition (Fig. 3, A to I). In the chemokine-bound CCR1, CCR2, and CCR5 structures, $E^{7.39}$ forms hydrogen bonds with the chemokine ligand (Fig. 3, A to D). In nonpeptide ligand-bound CCR2 and CCR5 structures, $Y^{1.39}$ forms hydrogen bonds with the ligand (Fig. 3, E and F). Consistent with that, $E^{7.39}$A or $Y^{1.39}$A substitution profoundly impaired the ligand-induced receptor activation (*8*–*10*, *31*, *32*). In the CCR8-nonpeptide agonist structures, $Y42^{1.39}$ makes a van der Waals interaction with the ligand, and $Y113^{3.32}$ forms a π-π interaction with the central benzene ring of the ligand (Fig. 2, C and E). Our mutagenesis and functional assay result showed that in addition to $E286^{7.39}$A as mentioned above, the $Y42^{1.39}$A and $Y113^{3.32}$A mutations also reduced agonist-induced activation in CCR8 substantially (Fig. 2, D and F).

Selectivity of nonpeptide ligand for CCR8

To clarify the selectivity of nonpeptide ligands to CKRs, we compared the amino acid sequence constituting the orthosteric pocket of CCR8 with other CC CKRs (Fig. 4A). We found that two residues, $Y114^{3.33}$ and $Y172^{4.64}$ of CCR8, are not conserved among CC CKRs but important for both LMD-009 and ZK 756326 binding (Fig. 4, B and C). To further validate this selectivity filter mechanism, we assessed the signaling activity of $Y114^{3.33}$A and $Y172^{4.64}$A mutations in CCR8 using cellular Ca^{2+} flux activation assays (*33*) in human embryonic kidney (HEK) 293T cells by cotransfecting $G_{\alpha15/16}$ and the receptor (Fig. 4, D and E, and Materials and Methods). $Y114^{3.33}$ mutation to alanine resulted in a profound reduction in CCR8 activation induced by ZK 756326 and LMD-009. Likewise, $Y172^{4.64}$ mutation to alanine led to reduction of the maximum activation effect for ZK 756326 (E_{max} is maximum effect) and the potency for LMD-009 [according to median effective concentration (EC_{50})]–induced CCR8 activation (Fig. 4, D and E, and table S3). Consistent with our findings, the double mutation ($Y114^{3.33}$A and $Y172^{4.64}$A) further impaired the agonist activity for LMD-009 and completely abolished the activation effect for ZK 756326. The two residues are not conserved in other CC CKRs (Fig. 4A), which may explain why the two agonists can selectively activate CCR8 (*20*).

However, the highly similar poses of ZK 756326 in CCR8 and maraviroc in CCR5 indicate an overall conserved binding pocket between CCR8 and CCR5 (fig. S5A). Contrary to the binding mode

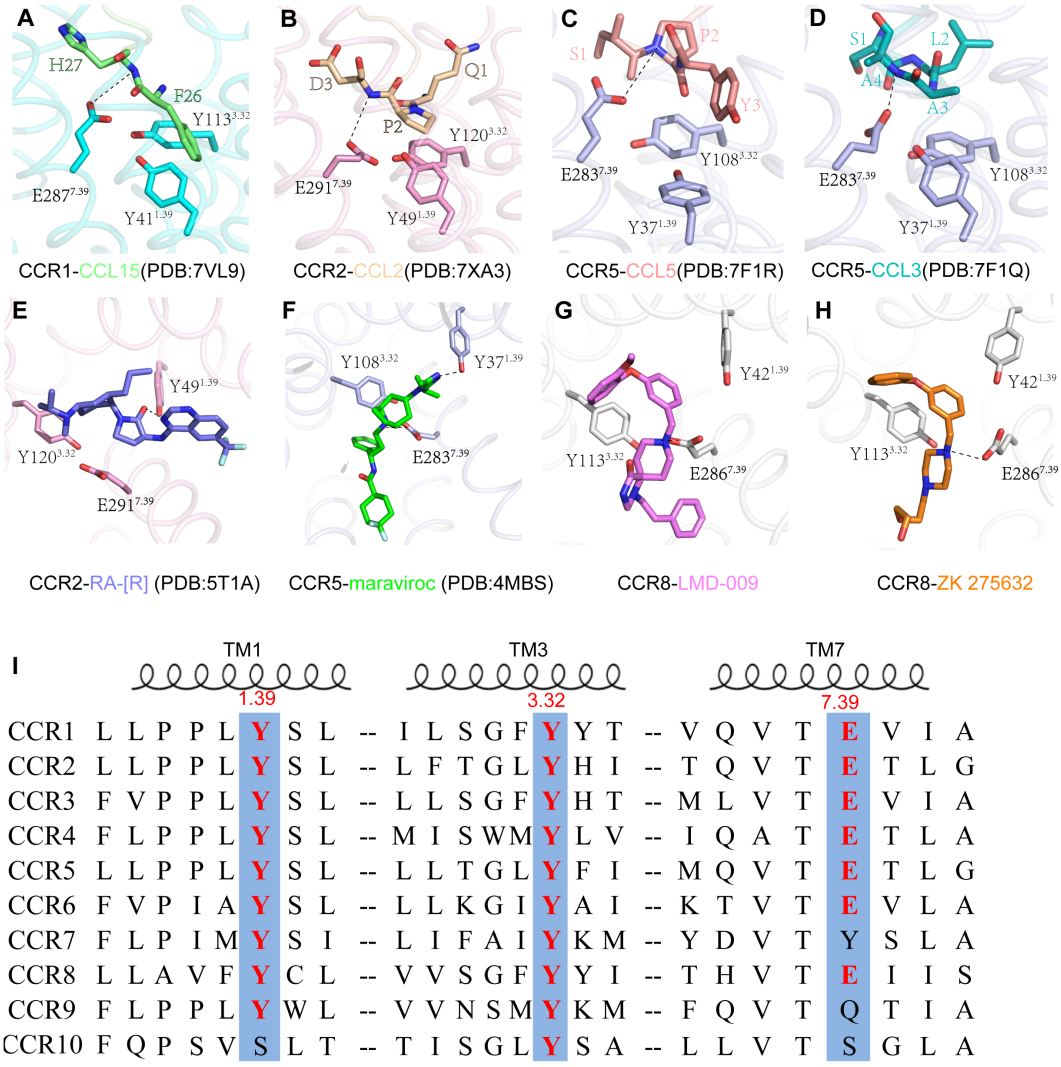

I

	TM1								TM3								TM7							
					1.39								3.32								7.39			
CCR1	L	L	P	P	L	**Y**	S	L	--	I	L	S	G	F	**Y**	Y	T	--	V	Q	V	T	**E**	V	I	A
CCR2	L	L	P	P	L	**Y**	S	L	--	L	F	T	G	L	**Y**	H	I	--	T	Q	V	T	**E**	T	L	G
CCR3	F	V	P	P	L	**Y**	S	L	--	L	L	S	G	F	**Y**	H	T	--	M	L	V	T	**E**	V	I	A
CCR4	F	L	P	P	L	**Y**	S	L	--	M	I	S	W	M	**Y**	L	V	--	I	Q	A	T	**E**	T	L	A
CCR5	L	L	P	P	L	**Y**	S	L	--	L	L	T	G	L	**Y**	F	I	--	M	Q	V	T	**E**	T	L	G
CCR6	F	V	P	I	A	**Y**	S	L	--	L	L	K	G	I	**Y**	A	I	--	K	T	V	T	**E**	V	L	A
CCR7	F	L	P	I	M	**Y**	S	I	--	L	I	F	A	I	**Y**	K	M	--	Y	D	V	T	**Y**	S	L	A
CCR8	L	L	A	V	F	**Y**	C	L	--	V	V	S	G	F	**Y**	Y	I	--	T	H	V	T	**E**	I	I	S
CCR9	F	L	P	P	L	**Y**	W	L	--	V	V	N	S	M	**Y**	K	M	--	F	Q	V	T	**Q**	T	I	A
CCR10	F	Q	P	S	V	**S**	L	T	--	T	I	S	G	L	**Y**	S	A	--	L	L	V	T	**S**	G	L	A

Fig. 3. CC CKR orthosteric pocket and the conserved $Y^{1.39}Y^{3.32}E^{7.39}$ motif. (**A** to **D**) Interactions between conserved $Y^{1.39}Y^{3.32}E^{7.39}$ motif in different CKRs with corresponding chemokines. CCR1-CCL15 (A), CCR2-CCL2 (B), CCR5-CCL15 (C), and CCR5-CCL3 (D). The hydrogen bonds are shown as dashed black line. (**E** to **H**) Interactions between conserved $Y^{1.39}Y^{3.32}E^{7.39}$ motif in different CKRs with nonpeptide ligands. The hydrogen bonds are shown as dashed black line. CCR2 and RA-[R] (E), CCR5-maraviroc (F), CCR8–LMD-009 (G), and CCR8–ZK 756326 (H). (**I**) Sequence alignment of $Y^{1.39}Y^{3.32}E^{7.39}$ motif and surrounded residues in the 10 human CC CKRs. $Y^{1.39}$, $Y^{3.32}$, and $E^{7.39}$ are shown in red, and the structurally equivalent positions are shown with a light blue background.

of ZK 756326 in CCR8, BMS-618 in CCR2 exhibits a different binding mode and only interacts with TM1 and TM7, without direct interaction with TM6 (fig. S5B). Notably, molecular docking analysis suggests that reported CCR8 potential nonpeptide ligands, AZ6 (*19*) and AZ084 (*34*), may occupy the orthosteric pocket in a similar manner, although with different chemical scaffolds (fig. S6, A and B). Among them, AZ084 is a clinical-stage small-molecule drug targeting CCR8 developed by AstraZeneca for the treatment of solid tumors. We performed the G protein dissociation (BRET assay) and Ca^{2+} flux assay for AZ084 (fig. S6, C to E, and table S3). The BRET and Ca^{2+} flux assay results suggest that AZ084 displays comparable activity to LMD-009 and ZK 756326, effectively activating the G protein signaling downstream of CCR8 (fig. S6, C and D, and table S3). Meanwhile, the two key amino acids, $Y114^{3.33}$ and $Y172^{4.64}$, when mutated to alanine, all impair the activity of AZ084, further confirming our docking results (fig. S6E and table S3).

Molecular basis for activation of CCR8

To elucidate the conformational changes associated with CCR8 activation, we compared the agonist-bound and G_i-coupled CCR8 structures with the inactive-state CCR2 and CCR5 structures. This is because, currently, only structures of CCR2 and CCR5 with nonpeptide antagonists bound to the orthosteric pockets are available within the CC CKRs (Fig. 5, A and B). Structural comparison revealed a large-scale conformational change at both cytoplasmic and extracellular regions that may elucidate the activation-related structural transformation on CCR8 (Fig. 5, A and B). Compared to inactive CCR2, G_i-coupled CCR8 adopts an outward movement of TM6 for about 6.0 Å (based on Cα of $A^{6.33}$) and an inward movement of TM5 for about 4.1 Å (based on Cα of $I^{5.61}$) at the cytoplasmic side (Fig. 5A). Compared to inactive CCR5, we only observed an outward movement of TM6 for about 6.1 Å (based on Cα of $A236^{6.33}$) in G_i-coupled CCR8 (Fig. 5B). In particular, critical structural elements

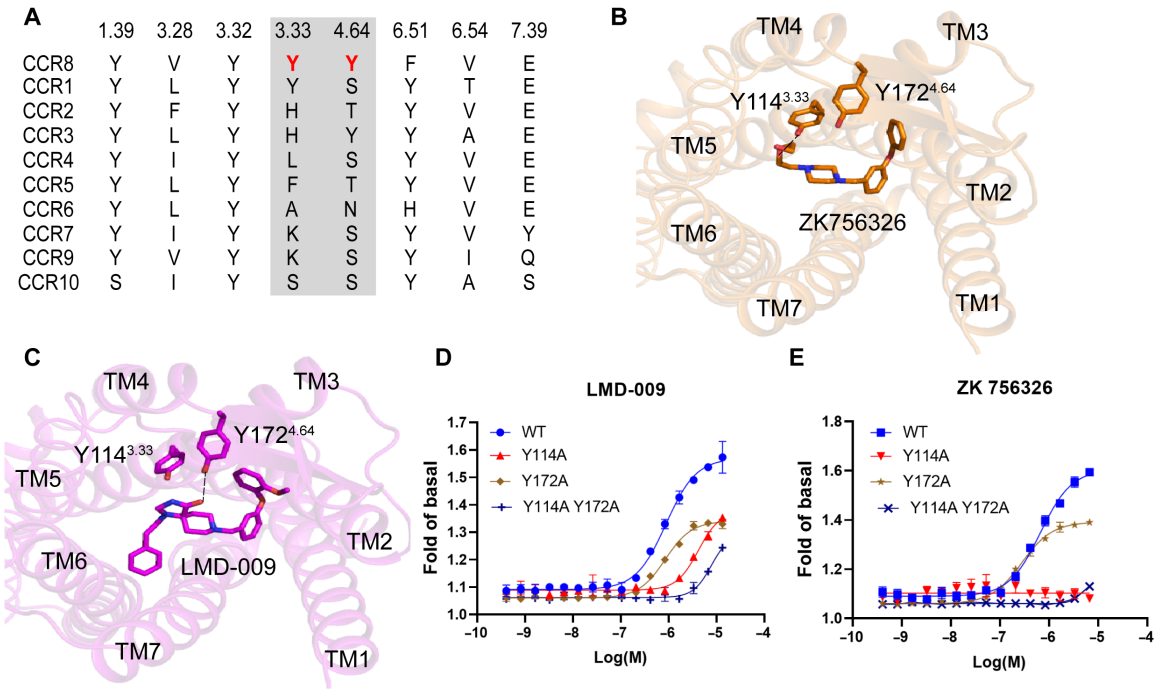

Fig. 4. Selectivity of nonpeptide ligand for CC CKRs. (**A**) Sequence alignment of human CCR8 orthosteric pocket with other nine human CC CKRs. Differential residues are labeled in gray shade. The residue 3.33 and residue 4.64 of CCR8 are shown in red font. (**B** and **C**) Two key residues in CCR8 for nonpeptide ligand selectivity: $Y^{3.33}$ and $Y^{4.64}$. The black dotted lines represent hydrogen bonds. (**D** and **E**) Functional effect of CCR8 mutation on CCR8 signaling activity was monitored by Ca^{2+} flux assay in HEK293 T cells, stimulated by LMD-009 (D) and ZK 756326 (E). Data points represent mean signal ± SD ($n = 3$). Data shown are representatives of three independent experiments. Fits to data points by a three-parameter response model are shown as solid lines.

in class A GPCR activation including the $D^{3.49}R^{3.50}Y^{3.51}$ motif, the toggle switch $W^{6.48}$, and the $P^{5.50}M^{3.40}F^{6.44}$ motif all undergo profound conformational changes during the activation of CCR8 (Fig. 5, C to F).

As maraviroc is a US Food and Drug Administration–approved drug acting as an antagonist on CCR5 and that it shows similar binding pose to ZK 756326, an agonist on CCR8, we next examined the ligand-binding pocket between the two structures to elucidate key molecular interactions that may potentially differentiate agonists from antagonists. In the maraviroc-bound CCR5 structure, the phenyl group of maraviroc is deeply inserted into the ligand-binding pocket and forms direct hydrophobic interaction with the toggle switch $W248^{6.48}$, thus preventing the downward swing of $W248^{6.48}$ and maintaining the receptor in its inactive state (Fig. 5, G and H). In the agonist-bound CCR8 complexes, the agonist interacts with $Y254^{6.51}$ through a hydrophobic interaction, triggering the transmission of signals to the toggle switch $W251^{6.48}$ located beneath. The downward swing of $W251^{6.48}$ is accompanied by conformational changes of residue $P210^{5.50}$ in the PIF motif (Fig. 5, E and I), and $R131^{3.50}$ in the DRY motif (Fig. 5, F and J).

$W^{6.48}$ is at the center of these conformational changes, establishing a connection between ligand binding and the helical movement associated with receptor activation through TM7 and TM6. This coordinated movement results in the opening of an intracellular crevice, facilitating G protein coupling (Fig. 5, C, D, G, and H). A subgroup of CC CKRs (CCR6, CCR7, CCR9, and CCR10) features a $Q^{6.48}$ residue at the toggle switch position. These receptors selectively bind to a limited number (one and two) of chemokines characterized by short N termini (four to nine residues). Intriguingly, the conformational changes during activation may not necessarily be initiated by ligand engagement with the core 7TM bundle. This observation underscores the distinctive "shallow" activation mechanism for these CC CKRs where the presence of a Q at residue 6.48 is notable (*35*). In contrast, CC CKRs featuring the conserved $W^{6.48}$ (CCR1, CCR2, CCR3, CCR4, CCR5, and CCR8) tend to be more promiscuous and preferentially recognize chemokines with long N termini (9 to 14 residues) (*36*).

CC CKR coupling with G_i protein

Structural superimposition enables us to understand the coupling mechanism of CC CKRs with the downstream G_i protein. Similar to other G_i protein complex structures, the C terminus of the α5 helix of the $G_{\alpha i}$ protein adopts a loop conformation, binding to the intracellular crevice of the 7TM bundle of CCR8 (*37*). The overall structures of CC CRK–G_i protein complexes are quite similar to each other (fig. S7, A and B), with the predominant binding mode following the canonical conformation as previously described (*38*). While the structures of CC CKRs with G protein complexes exhibit a high degree of similarity (fig. S7, A and B), notable structural differences were observed in the conformation of $G_{\alpha i}$ protein, characterized by the maximal difference between two CC CKRs for an about 4-Å shift of α5 helix (fig. S7C) (measured at the G_α atoms of $N331^{H5.03}$) and an about 19-Å shift of the αN helix (fig. S7D) (measured at the G_α atoms of $E8^{HN.32}$). The structural changes of G_i protein varying from different CC CKRs may be due to the subtle conformational differences in the intracellular end of TM5/6 and ICL2/3 of the receptors.

In all three of our CCR8-G_i complex structures, CCR8 shared highly similar interaction profiles with $G_{\alpha i}$ (Fig. 6A). The major contacts to α5 helix of $G_{\alpha i}$ protein come from TM3, TM6, ICL2, and

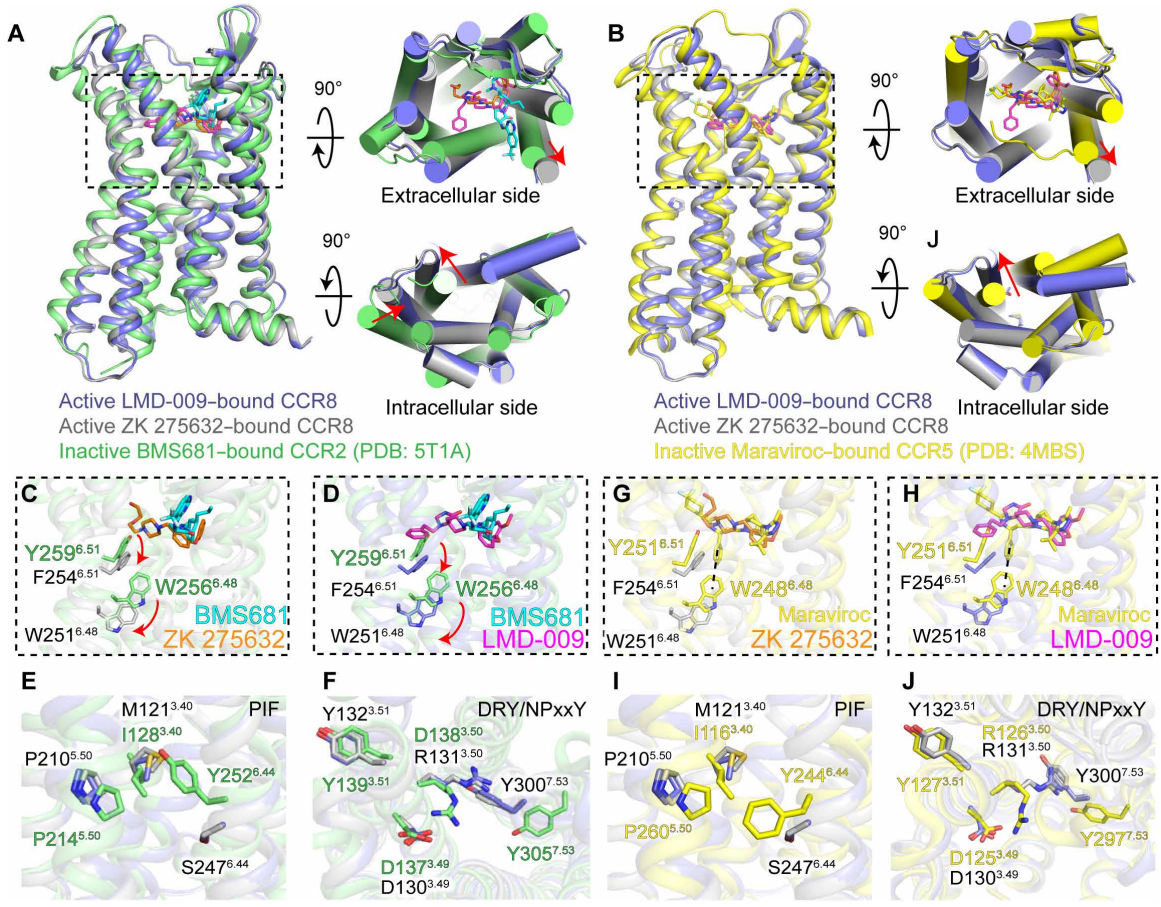

Fig. 5. Molecular basis for activation of CCR8. (**A**) Agonist-bound CCR8 (active state) structures superimposed on the inactive CCR2 structure (CCR2-BMS681, PDB: 5T1A, green color). (**B**) Agonist-bound CCR8 (active state) structures superimposed on the inactive CCR5 structure (CCR5-maraviroc, PDB: 4MBS, yellow color). (**C** to **F**) Comparing the conformational changes in the conserved motif between activated CCR8 and inactive CCR2. The movement of $F254^{6.51}$ and the downward swing of $W251^{6.48}$ are indicated by red arrows. (**G** to **J**) Comparing the conformational changes in the conserved motif between activated CCR8 and inactive CCR5. LMD-009–bound CCR8 is shown in blue, and ZK 756326–bound CCR8 is shown in gray.

ICL3 of CCR8 (Fig. 6, A and B). Previous structural characterization of CC CKRs in association with G proteins reveals that the residues within the ICL2 region establish highly conserved interactions with the α5 helix of $G_{\alpha i}$ (Fig. 6C). The ICL2 of CCR8 forms a two-turn α-helical structure in which $V139^{ICL2}$ inserts into a hydrophobic pocket formed by αN-β1 loop and α5 helix of $G_{\alpha i}$ protein (fig. S8). The $G_{\alpha i}$ coupling is further stabilized by hydrogen bonds between ICL3 and α5, including $Q229^{ICL3}$ with $D341^{H5.31}$, and $H231^{ICL3}$ with $K317^{h4s6.11}$ (Fig. 6B) and a series of hydrophobic residues from ICL2, such as $A138^{ICL2}$, $V139^{ICL2}$, and $R145^{ICL2}$ forming interactions with $L194^{s3.01}$, $I343^{H5.15}$, and $N347^{H5.15}$ in $G_{\alpha i}$ (Fig. 6B) [superscripts refer to the common G_{α} numbering system, hereafter (*39*)]. Consistent with the structural finding, mutagenesis and cellular functional assays showed that most of the mutations at the interface reduced the ligand-binding activity of CCR8 (Fig. 6, D and E, and table S2). Previous reports have indicated that the ICL2-$G_{\alpha i}$ interface plays a more important role than the ICL3-$G_{\alpha i}$ interface in the coupling of CKRs with G proteins (*9*). However, in CCR8, both the ICL2-$G_{\alpha i}$ interface and the ICL3-$G_{\alpha i}$ interface are equally essential for G protein coupling.

DISCUSSION

In this study, we determined the cryo-EM structures of CCR8-G_i complexes in both ligand-bound and ligand-free states, providing the insight into the mechanism by which nonpeptide agonists recognize the CKR. Nonpeptide ligands of CC CKRs typically exhibit a common pharmacophore featuring a centrally positioned, positively charged amine, with Glu-VII:06 serving as an anchoring point (*30*). Our findings indicate that the lack of conservation in $Y114^{3.33}$ and $Y172^{4.64}$ among the CC CKRs could potentially contribute to the selectivity of nonpeptide ligands, as both residues play crucial roles in the binding of the two ligands as revealed in our structures and functional validation.

On the other hand, the conserved $Y^{1.39}Y^{3.32}E^{7.39}$ motif plays a vital role in the recognition of nonpeptide ligands and chemokines within the orthosteric binding pocket. However, chemokines and nonpeptide ligands bind to receptors in very different ways. The binding of chemokines to receptors is a classical two-site model involving two main interaction sites: (i) chemokine recognition site 1 (CRS1), where the N terminus of the receptor interacts with the globular core of the chemokine, and (ii) chemokine recognition site 2 (CRS2),

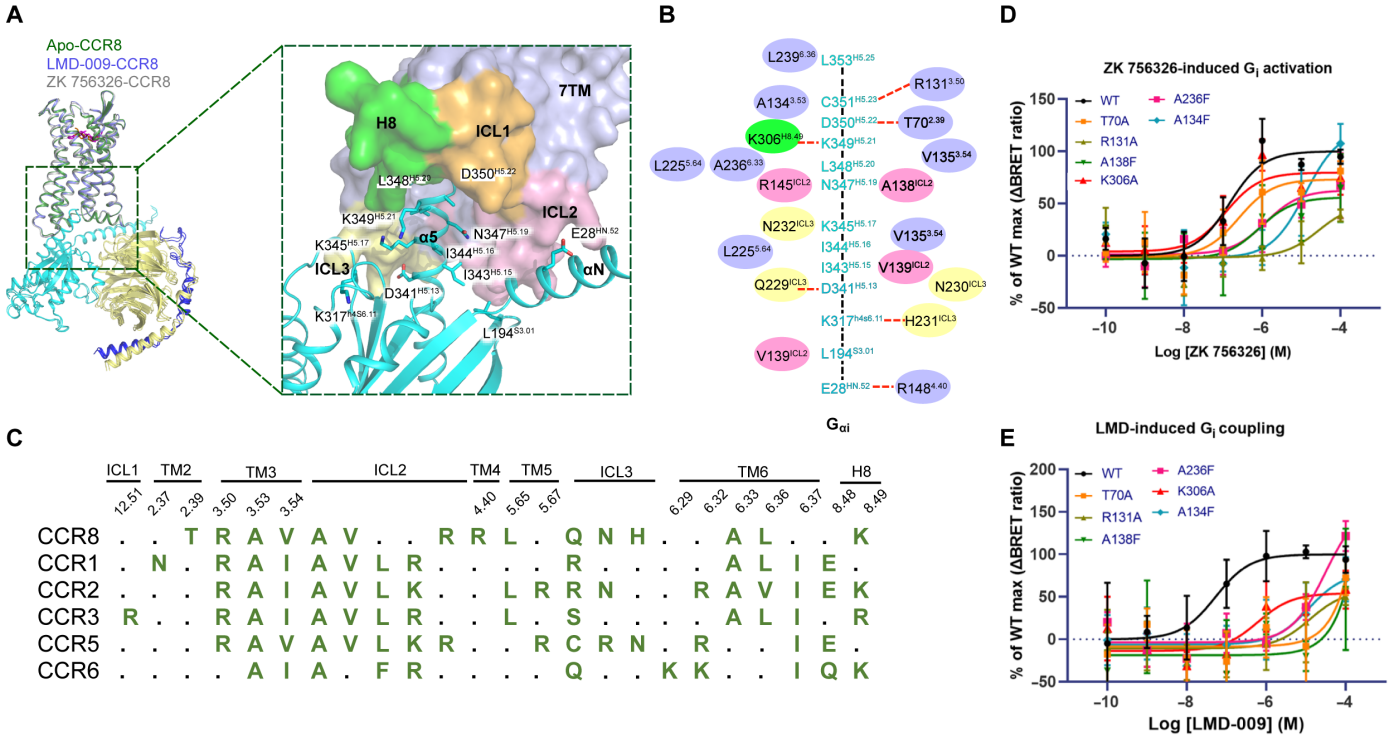

Fig. 6. The interface between G protein and CC CKRs. (**A**) Overall comparison of three CCR8-G_i structures by superposition on CCR8 (left); insertion of the α5-helix ($G_{\alpha i}$, cyan) into the CCR8 TMD represented as surface (right). (**B**) Molecular interactions between CCR8 and $G_{\alpha i}$ shown in 2D. The interacting residues on $G_{\alpha i}$ and CCR8 are shown in cyan and black, respectively. Residues on 7TM, ICL2, ICL3, and H8 are shown in light blue, pink, yellow, and cyan circles, respectively. Hydrogen bonds are highlighted with dashed red lines. (**C**) Sequence alignment of CCR1, CCR2, CCR3, CCR5, CCR6, and CCR8 in the regions of G protein interface. (**D** and **E**) Mutagenesis of G protein interface residues and functional measurement ($G_{\alpha\beta\gamma}$ heterotrimer dissociation by BRET assay) of ZK 756326 (D)– or LMD-009 (E)–induced G_i activation of CCR8. Data are means ± SEM.

where the N terminus of the chemokine interacts with the transmembrane-binding pocket of the receptor (*40*). Structure-guided discovery of the $Y^{1.39}Y^{3.32}E^{7.39}$ motif that contributes to both chemokine and nonpeptide recognition on CKRs is thus of great value for design of ligands to interfere chemokine binding for broad therapeutic applications particularly in the cancer immunotherapy.

Previous studies report two nonpeptide ligand-binding pockets in the CKRs, the orthosteric pocket and an allosteric pocket usually located on the receptor's intracellular side. It is known that some CKRs have an intracellularly located allosteric pocket, which has been observed in CCR2 (*32*), CCR7 (*41*), and CCR9 (PDB: 5T1A, 6QZH, and 5LWE) (*42*). The interactions between allosteric antagonist and the receptor partially obstruct the G protein–binding site, impeding the conformational changes necessary for receptor activation (fig. S9). Previous strategies for targeting CKRs for drug discovery may involve identifying ligands that bind to the allosteric pockets for better selectivity. For example, maraviroc was initially found as an allosteric modulator, but its complex structure with CCR5 indicates a binding site in the classical orthosteric pocket. Our nonpeptide agonist–bound CCR8 structures unveil a very similar binding pose with maraviroc. Our structural analysis reveals the binding sites of nonpeptide ligands overlapping with those of chemokines, facilitated by the conserved $Y^{1.39}Y^{3.32}E^{7.39}$ motif. This finding uncovers the mechanism of action for nonpeptide ligand. Furthermore, our structures pinpoint the selectivity mechanism for the nonpeptide ligand recognition in CCR8. Therefore, we propose that both the intracellular allosteric pocket and orthosteric pocket hold important value for the design of selective ligands and the discovery of drugs targeting CCR8.

In summary, the cryo-EM structures presented in this study offer valuable insights into the recognition of nonpeptide agonists and provide direct structural evidence for G protein activation by CCR8. Despite CCR8 being considered a potential target for cancer immunotherapy and autoimmune diseases, the progress in developing CCR8-targeted drugs has been limited. Through conservation analysis, our findings provide additional insights into the molecular mechanisms underlying the recognition of nonpeptide ligands by other CKRs. Together, these findings present insightful prospects for the structure-based discovery of drug molecules for CCR8 as well as for the broader CKR family.

MATERIALS AND METHODS

Constructs and protein expression

The codon-optimized nucleotide of WT CCR8 (UniProt ID P51685) was synthesized by GenScript. For the cryo-EM study, the human CCR8 gene was cloned into a modified pFastBac1 Vector (Invitrogen) with a hemagglutinin signal peptide followed by a Flag tag at the N terminus and fused with a LgBiT subunit (*43*) at the C terminus via a 15× GS linker containing a 3C protease cleavage site and 10× His tag. A dominant-negative Gαi1 ($DNG_{\alpha i1}$) was generated by site-directed mutagenesis to decrease the affinity of nucleotide binding, introducing three mutations, S47N, G203A, and A236S. The human $G_{\beta 1\gamma 2}$ gene with an SmBiT at the C terminus of $G_{\beta 1}$ was cloned into

the pFastDual vector (Invitrogen). The modified CCR8 was coexpressed with $DNG_{\alpha i1}$ and $G_{\beta 1\gamma 2}$ in *Trichoplusia ni* Hi5 insect cells (Invitrogen) using Bac-to-Bac Baculovirus Expression System (Invitrogen). *T. ni* Hi5 cells were infected at a cell density of 2×10^6 to 2.5×10^6 cells/ml with three separated virus (multiplicity of infection = 5) preparations for CCR8, $DNG_{\alpha i1}$, and $G_{\beta 1\gamma 2}$ at a ratio of 2:2:1. The infected cells were cultured at 27°C for 48 hours before collection by centrifugation, and the cell pellets were stored at −80°C for future use.

Expression and purification of scFv16

The expression and purification of scFv16 were the same as previously described (*26*). The codon-optimized nucleotide sequence of scFv16 was synthesized by GenScript and subcloned into an expression vector pFastBac1 with an 8× His tag at the C terminus. In brief, scFv16 was overexpressed and secreted into the culture medium of transfected *T. ni* Hi5 cells and purified by Ni–nitrilotriacetic acid chromatography. The elution was purified by size exclusion chromatography on a Superdex 200 Increase 10/300 GL column (GE Healthcare). Then, the monomeric fraction was concentrated, flash-frozen, and stored at −80°C until use.

Purification of ligand-bound CCR8-G_i and apo-CCR8-G_i complex

All purification steps were performed on ice. For cell lysis, frozen cell pellets were thawed in the hypotonic buffer containing 10 mM Hepes (pH 7.5), 10 mM $MgCl_2$, and 20 mM KCl with EDTA-free complete protease inhibitor cocktail tablets (Roche). The CCR8-G_i complex was generated in membranes by adding 2 U of apyrase (NEB). After overnight incubation at 4°C, the supernatant was removed following centrifugation at 35,000 rpm for 30 min. Then, the membranes were solubilized in the buffer consisting of 50 mM Hepes (pH 7.5), 100 mM NaCl, 1% (w/v) lauryl maltose neopentyl glycol (LMNG; Anatrace), 0.2% (w/v) cholesteryl hemisuccinate (CHS) (Sigma-Aldrich), and 1 U of apyrase at 4°C for 2.5 hours. The supernatant was then separated by ultracentrifugation at 35,000 rpm for 30 min and incubated with TALON IMAC resin (Clontech, 600 μl of resin per 1 liter of biomass) and 20 mM imidazole overnight at 4°C. The resin was washed with 15 column volumes (CVs) of washing buffer I containing 25 mM Hepes (pH 7.5), 100 mM NaCl, 5% (v/v) glycerol, 0.1% (w/v) LMNG, 0.02% (w/v) CHS, 30 mM imidazole, and 15 CVs of washing buffer II containing 25 mM Hepes (pH 7.5), 100 mM NaCl, 5% (v/v) glycerol, 0.03% (w/v) LMNG, 0.006% (w/v) CHS, and 50 mM imidazole. The protein was eluted with 3 CVs of elution buffer containing 25 mM Hepes (pH 7.5), 100 mM NaCl, 10% (v/v) glycerol, 0.01% (w/v) LMNG, 0.002% (w/v) CHS, and 250 mM imidazole. The eluate (CCR8-G_i complex) was mixed with purified scFv16 at a 1:1.5 ratio for 0.5 hours, then concentrated, and injected onto a Superdex200 10/300 GL column (GE Healthcare) equilibrated in a buffer containing 20 mM Hepes (pH 7.5), 100 mM NaCl, 0.00075% (w/v) LMNG, 0.00025% glyco-diosgenin (GDN), 0.0001% (w/v) CHS, and 100 μM tris(2-carboxyethyl)phosphine (TCEP). The peak fractions of the complex were collected and concentrated to 2.5 mg ml^{-1} with a 100-kDa cutoff concentrator (Millipore) for electron microscopy experiments. The same strategy was used for the ligand-bound CCR8-G_i complex, except for adding 10 μM ZK 756326 or LMD-009 to each purification step.

Cryo-EM grid preparation and data collection

The purified ligand-bound or apo-CCR8-G_i (3.5 μl) was applied to a glow-discharged Quantifoil R1.2/1.3 holey carbon grid at a concentration of approximately 3 mg/ml in each purification buffer. The grids were then plunged into liquid ethane using a Thermo Fisher Scientific Vitrobot Mark IV, transferred to liquid nitrogen, and stored for data collection. The datasets were acquired using a Titan Krios 300 kV electron microscope (Thermo Fisher Scientific, USA) equipped with a GIF Quantum energy filter (20 eV energy slit width, Gatan Inc., USA). The CCR8 datasets were obtained using a K3 camera (Gatan) with a nominal magnification of 105,000 (calibrated pixel size: 0.832 Å per pixel) and an exposure rate of 15 $e^-/pixel^2$ per second. The images were recorded in super-resolution counting mode using SerialEM, which used the beam image shift acquisition method with one image captured near the edge of each hole. During data collection, a 50-μm C2 aperture was always present. The defocus values ranged from −0.7 to −2.2 μm. Each movie stack consisted of 40 frames, with a total dose of 60 $e^-/Å^2$. All datasets were collected in the Bio-EM Center, ShanghaiTech University (Shanghai, China).

Cryo-EM data processing

For the apo-CCR8-G_i complex, 5658 movies were recorded and processed with cryoSPARC v.4.2.1 (*44*). Patch motion correction was used for beam-induced motion correction. Then, contrast transfer function (CTF) parameters for each dose-weighted micrograph were estimated by patch CTF estimation. Next, 400 images were selected to do auto-blob picking, and 224,398 particles were extracted to do 2D classification. Then, 40,691 particles in good 2D patterns were selected to do deep-learn training in topaz. A total of 3,664,205 particles were picked out in topaz extraction and used to do 2D classification. A total of 702,809 particles were selected from good 2D classification to construct initial models and then 3D classification in heterogeneous refinement in cryoSPARC. A total of 527,677 particles were selected for final homogeneous refinement followed by nonuniform refinement and local refinement in cryoSPARC, resulting in a density map with a nominal resolution of 2.74 Å [determined by gold-standard Fourier shell correlation (FSC), 0.143 criteria]. While checking the map, we found that the density of several transmembrane helices was disordered near the extracellular loop (ECL) part of CCR8. So, one more cycle of 3D classification with a mask focused on the ECL part of CCR8 was performed. Last, 27,420 particles were selected to do heterogeneous refinement and local refinement, resulting in a density map with a nominal resolution of 3.31 Å, which has a much clear density in the ECL part of CCR8. Estimation of the local resolution was performed with local resolution estimation in cryoSPARC. Both density maps were performed by automatic masking and local sharpening in DeepEMhancer (*45*) to optimize the local density.

For the LMD-009–CCR8–G_i complex, 3617 movies were recorded and processed with cryoSPARC v.4.2.1 (*44*). Patch motion correction was used for beam-induced motion correction. Then, CTF parameters for each dose-weighted micrograph were estimated by patch CTF estimation. A total of 2,607,988 particles were picked out in topaz extraction with a training model from a dataset of apo-CCR8-Gi and used to do 2D classification. A total of 1,008,163 particles were selected from good 2D classification to construct initial models and do the subsequent two cycles of 3D classification in heterogeneous refinement in cryoSPARC. A class with 419,265 particles was selected to do homogeneous refinement, followed by nonuniform refinement. A density map with a nominal resolution of 2.79 Å was obtained. Then, 3D classification with a focus mask in the ligand region was performed to optimize the density of the ligand. Last, 105,277 particles

were selected for the final homogeneous refinement followed by nonuniform refinement and local refinement in cryoSPARC, resulting in a density map with a nominal resolution of 2.96 Å for a complex of LMD-009–CCR8–G_i (determined by gold-standard FSC, 0.143 criteria). Estimation of the local resolution was performed with local resolution estimation in cryoSPARC. Both density maps were performed by automatic masking and local sharpening in DeepEMhancer to optimize the local density.

For the ZK 756326–CCR8–G_i complex, 5769 movies were recorded and processed with cryoSPARC v.4.2.1 (*44*). Patch motion correction was used for beam-induced motion correction. Then, CTF parameters for each dose-weighted micrograph were estimated by patch CTF estimation. A total of 4,708,145 particles were picked in topaz extraction with a training model from a dataset of apo-CCR8-G_i and used to do 2D classification. A total of 707,420 particles were selected from good 2D classes to construct four initial models, and then one cycle of 3D classification in heterogeneous refinement in cryoSPARC was performed. Two sets of 3D classes with 364,306 particles were selected to do homogeneous refinement, followed by nonuniform refinement and local refinement. A density map with a nominal resolution of 2.84 Å was obtained. Then, 3D classification with a focus mask in the ligand region was performed to optimize the density of the ligand. Last, 124,576 particles were selected to do final homogeneous refinement followed by nonuniform refinement and local refinement in cryoSPARC, resulting in the density map with a nominal resolution of 3.06 Å for the complex of ZK 756326–CCR8–G_i (determined by gold-standard FSC, 0.143 criteria). Estimation of the local resolution was performed with local resolution estimation in cryoSPARC. Both density maps were performed by automatic masking and local sharpening in DeepEMhancer to optimize the local density.

Model building and refinement

The initial model of CCR8 was obtained from the AlphaFold protein structure database, and the initial G protein complex was extracted from PDB ID 6LFM. Each part of the target models was docked into the electron microscopy density using UCSF Chimera v.1.15 (*46*), followed by iterative manual adjustment and rebuilding in Coot v.0.9.8 (*47*), and refinement in real space in Phenix v.1.20 (*48*). The model statistics were validated using MolProbity v.4.2 (*49*). Structural figures were prepared in UCSF Chimera, Chimera X v.1.2.4, and PyMOL v.2.5.1 (http://pymol.org). The final refinement statistics are provided in table S1.

BRET2 assay

To measure the dissociation of $G_{\alpha\beta\gamma}$ heterotrimer directly, we applied the BRET2 assay system as reported before (*23*). In brief, HEK293T cells were plated in a six-well plate. After 2 hours, cells were transiently cotransfected with plasmids encoding WT or mutated CCR8 together with G_i BRET probe ($G_{\alpha i1}$-RLuc8, $G_{\beta 3}$, $G_{\gamma 9}$-GFP2) using Lipofectamine 2000 reagent (Life Technologies). $A_{2A}R$ that does not couple to G_i proteins was used as a negative control, and GPR20 that constitutively couples to G_i proteins were used as a positive control for the G_i BRET assay. Twenty hours after transfection, cells were distributed into a 96-well microplate (30,000 to 50,000 cells per well) and incubated for an additional 24 to 36 hours at 37°C. For the constitutive activity measurement, white backings (PerkinElmer) were applied to the plate bottoms, and the transfected cells were washed once with Hanks' balanced salt solution (HBSS) and supplemented with 100 μl of 5 μM coelenterazine 400a (Nanolight Technologies). Plates were read in Tristar5 plate reader (Berthold) with 410-nm (RLuc8–coelenterazine 400a) and 515-nm (GFP2) emission filters with an integration time of 0.8 s per well. The GFP2 emission to RLuc8 emission ratio was used to compute the BRET2 ratios. For the drug measurement, white backings were applied to the plate bottoms, and the growth medium was replaced by 40 μl of HBSS. After 5 min, 40 μl of indicated agonists was added in for another 5 min and then supplemented with 20 μl of 25 μM coelenterazine 400a. Plates were read in Tristar 5 (PerkinElmer) with 410-nm (RLuc8–coelenterazine 400a) and 515-nm (GFP2) emission filters with an integration time of 0.8 s per well. The GFP2 emission to RLuc8 emission ratio was used to compute the BERT2 ratios. ΔBRET represents the change of BRET value. ΔBRET = BRET ratio (GPCR with G protein sensor) − BRET ratio (only G protein sensor). We carried out nonlinear regression analysis using a sigmoidal dose response in GraphPad v 8.2.1 Prism to calculate the values of E_{max}. All concentration-response curves were fit to a parameter logistic equation in GraphPad v 8.2.1 Prism. BRET2 concentration response curves were analyzed either as raw net BRET (fit E_{max} − fit baseline) or by normalizing to a reference agonist for each experiment. E_{max} and transduction coefficient values were calculated by analysis of variance (ANOVA) (*F* test of curve fit, one-way ANOVA, or two-way ANOVA). Post hoc pairwise comparisons used Dunnett's-adjusted *P* values to control for multiple comparisons. The significance threshold was set at $\alpha = 0.05$.

Cell surface expression for each mutant was monitored by a fluorescence-activated cell sorting assay. In brief, the expressed cells were incubated with mouse anti-Flag [M2–fluorescein isothiocyanate (FITC)] antibody (Sigma-Aldrich) for 20 min at 4°C, and then a ninefold excess of phosphate-buffered saline was added to cells. Last, the surface expression of CCR8 or other receptors was calculated by detecting the fluorescent intensity of FITC using a Guava EasyCyte HT system (Millipore) (tables S2 and S3).

Ca^{2+} flux assay

HEK293 T cells were seeded at a density of 1×10^6 cells in 10-cm dishes overnight at 37°C in Dulbecco's modified Eagle's medium (DMEM; Life Technologies) containing 10% (v/v) fetal bovine serum (FBS; Gibco). On the day of transfection, 2.0 μg of plasmid DNA of CCR8 WT or its mutant plasmids was cotransfected to the cells with 2.0 μg of $G_{\alpha 15/16}$ plasmid using Lipofectamine 2000 transfection reagent. The cells grew for 24 hours in the incubator. The cells were then seeded into poly-L-lysine–coated 384-well black plates (Greiner) with DMEM supplemented with 1% dialyzed FBS (Gibco) at a density of 10,000 to 15,000 cells in 30 μl of medium per well and incubated for 4 to 6 hours at 37°C in 5% carbon dioxide incubator. Before assay detection, growth medium was removed, and cells were loaded with 20 μl per well of 1× Fluo-4 direct calcium dye (prepared in HBSS buffer) (Invitrogen) and incubated for 1 hour at 37°C in the dark. FLIPR was programmed to take 10 readings (1 read per second), initially as a baseline before the addition of 10 μl of 4× LMD-009, ZK 756326, AZ084 solution (prepared in HBSS buffer with 0.1% bovine serum albumin), and dimethyl sulfoxide as negative control. The fluorescence intensity was recorded for 2 min after addition of drug. Data were analyzed by nonlinear regression using GraphPad Prism 8.0. Agonist responses were defined as the maximum Ca^{2+} flux fluorescence signal divided by that of a control well with cells treated with buffer only.

Molecular docking

Molecular docking was performed using Schrödinger software. Processing of the protein structure was performed with the Protein Preparation Wizard (https://schrodinger.com/science-articles/protein-preparation-wizard); conversion of ligands from 2D to 3D structures was performed using LigPrep (https://schrodinger.com/products/ligprep); docking of AZ6 and AZ084 was performed with Glide 7.6 (https://schrodinger.com/products/glide) in standard precision, in which docking of AZ084 was performed with the Induced Fit Docking tool (https://schrodinger.com/science-articles/docking-and-scoring). The cartoons of all structures were generated by PyMOL.

Supplementary Materials

This PDF file includes:

Figs. S1 to S9
Tables S1 to S3

REFERENCES AND NOTES

1. P. M. Murphy, M. Baggiolini, I. F. Charo, C. A. Hébert, R. Horuk, K. Matsushima, L. H. Miller, J. J. Oppenheim, C. A. Power, International union of pharmacology. XXII. Nomenclature for chemokine receptors. *Pharmacol. Rev.* **52**, 145–176 (2000).
2. J. W. Griffith, C. L. Sokol, A. D. Luster, Chemokines and chemokine receptors: Positioning cells for host defense and immunity. *Annu. Rev. Immunol.* **32**, 659–702 (2014).
3. G. Lazennec, A. Richmond, Chemokines and chemokine receptors: New insights into cancer-related inflammation. *Trends Mol. Med.* **16**, 133–144 (2010).
4. X. Du, F. Li, C. Zhang, N. Li, H. Huang, Z. Shao, M. Zhang, X. Zhan, Y. He, Z. Ju, W. Li, Z. Chen, S. Ying, H. Shen, Eosinophil-derived chemokine (hCCL15/23, mCCL6) interacts with CCR1 to promote eosinophilic airway inflammation. *Signal Transduct. Target Ther.* **6**, 91 (2021).
5. E. J. Fernandez, E. Lolis, Structure, function, and inhibition of chemokines. *Annu. Rev. Pharmacol. Toxicol.* **42**, 469–499 (2002).
6. S. Zhao, B. Wu, R. C. Stevens, Advancing chemokine GPCR structure based drug discovery. *Structure* **27**, 405–408 (2019).
7. A. Steen, O. Larsen, S. Thiele, M. M. Rosenkilde, Biased and g protein-independent signaling of chemokine receptors. *Front. Immunol.* **5**, 277 (2014).
8. Z. Shao, Q. Shen, B. Yao, C. Mao, L. N. Chen, H. Zhang, D. D. Shen, C. Zhang, W. Li, X. du, F. Li, H. Ma, Z. H. Chen, H. E. Xu, S. Ying, Y. Zhang, H. Shen, Identification and mechanism of G protein-biased ligands for chemokine receptor CCR1. *Nat. Chem. Biol.* **18**, 264–271 (2022).
9. Z. Shao, Y. Tan, Q. Shen, L. Hou, B. Yao, J. Qin, P. Xu, C. Mao, L. N. Chen, H. Zhang, D. D. Shen, C. Zhang, W. Li, X. du, F. Li, Z. H. Chen, Y. Jiang, H. E. Xu, S. Ying, H. Ma, Y. Zhang, H. Shen, Molecular insights into ligand recognition and activation of chemokine receptors CCR2 and CCR3. *Cell Discov.* **8**, 44 (2022).
10. H. Zhang, K. Chen, Q. Tan, Q. Shao, S. Han, C. Zhang, C. Yi, X. Chu, Y. Zhu, Y. Xu, Q. Zhao, B. Wu, Structural basis for chemokine recognition and receptor activation of chemokine receptor CCR5. *Nat. Commun.* **12**, 4151 (2021).
11. X. Han, Constitutively active chemokine CXC receptors. *Adv. Pharmacol.* **70**, 265–301 (2014).
12. L. Wang, D. L. Simons, X. Lu, T. Y. Tu, S. Solomon, R. Wang, A. Rosario, C. Avalos, D. Schmolze, J. Yim, J. Waisman, P. P. Lee, Connecting blood and intratumoral T(reg) cell activity in predicting future relapse in breast cancer. *Nat. Immunol.* **20**, 1220–1230 (2019).
13. H. L. Tiffany, L. L. Lautens, J. L. Gao, J. Pease, M. Locati, C. Combadiere, W. Modi, T. I. Bonner, P. M. Murphy, Identification of CCR8: A human monocyte and thymus receptor for the CC chemokine I-309. *J. Exp. Med.* **186**, 165–170 (1997).
14. J. Cinier, M. Hubert, L. Besson, A. di Roio, C. Rodriguez, V. Lombardi, C. Caux, C. Ménétrier-Caux, Recruitment and expansion of tregs cells in the tumor environment-how to target them? *Cancers (Basel)* **13**, 1852 (2021).
15. D. B. Hoelzinger, S. E. Smith, N. Mirza, A. L. Dominguez, S. Z. Manrique, J. Lustgarten, Blockade of CCL1 inhibits T regulatory cell suppressive function enhancing tumor immunity without affecting T effector responses. *J. Immunol.* **184**, 6833–6842 (2010).
16. H. L. Li, L. H. Wang, Y. L. Hu, Y. Feng, X. H. Li, Y. F. Liu, P. Li, Q. S. Mao, W. J. Xue, Clinical and prognostic significance of CC chemokine receptor type 8 protein expression in gastrointestinal stromal tumors. *World J. Gastroenterol.* **26**, 4656–4668 (2020).
17. L. R. Y. Zong, O. A. Adelakun, I. Barman, J. R. Campbell, S. J. Z. Diong, F. Findeisen, D. M. Greenawalt, R. Jain, A. D. Jhatakia, J. K. Lee, Peter Sung Keun Lee, L. Liang, K. Lu, B. Mcdonald, P. B. Mesko, A. Rajpal, S. Sambanthamoorthy, M. J. Selby, N. O. Siemers, P. Strop, G. A. Terracina, W. X. Tao, Anti-CCR8 antibodies for treating cancer. WO 2021/194942 A1
18. Y. Barsheshet, G. Wildbaum, E. Levy, A. Vitenshtein, C. Akinseye, J. Griggs, S. A. Lira, N. Karin, CCR8(+)FOXp3(+) T(reg) cells as master drivers of immune regulation. *Proc. Natl. Acad. Sci. U.S.A.* **114**, 6086–6091 (2017).
19. L. Liu, J. Doijen, T. D'huys, Y. Verhaegen, W. Dehaen, S. de Jonghe, D. Schols, T. van Loy, Biological characterization of ligands targeting the human CC chemokine receptor 8 (CCR8) reveals the biased signaling properties of small molecule agonists. *Biochem. Pharmacol.* **188**, 114565 (2021).
20. P. C. Jensen, R. Nygaard, S. Thiele, A. Elder, G. Zhu, R. Kolbeck, S. Ghosh, T. W. Schwartz, M. M. Rosenkilde, Molecular interaction of a potent nonpeptide agonist with the chemokine receptor CCR8. *Mol. Pharmacol.* **72**, 327–340 (2007).
21. C. A. Haskell, R. Horuk, M. Liang, M. Rosser, L. Dunning, I. Islam, L. Kremer, J. Gutiérrez, G. Marquez, C. Martinez-A, M. J. Biscone, R. W. Doms, S. Ribeiro, Identification and characterization of a potent, selective nonpeptide agonist of the CC chemokine receptor CCR8. *Mol Pharmacol.* **69**, 309–316 (2006).
22. D. Alvarez Arias, J. M. Navenot, W.-B. Zhang, J. Broach, S. C. Peiper, Constitutive activation of CCR5 and CCR2 induced by conformational changes in the conserved TXP motif in transmembrane helix 2. *J. Biol. Chem.* **278**, 36513–36521 (2003).
23. R. H. J. Olsen, J. F. DiBerto, J. G. English, A. M. Glaudin, B. E. Krumm, S. T. Slocum, T. Che, A. C. Gavin, J. D. McCorvy, B. L. Roth, R. T. Strachan, TRUPATH, an open-source biosensor platform for interrogating the GPCR transducerome. *Nat. Chem. Biol.* **16**, 841–849 (2020).
24. X. Lin, B. Chen, Y. Wu, Y. Han, A. Qi, J. Wang, Z. Yang, X. Wei, T. Zhao, L. Wu, X. Xie, J. Sun, J. Zheng, S. Zhao, F. Xu, Cryo-EM structures of orphan GPR21 signaling complexes. *Nat. Commun.* **14**, 216 (2023).
25. A. J. Kooistra, S. Mordalski, G. Pándy-Szekeres, M. Esguerra, A. Mamyrbekov, C. Munk, G. M. Keserű, D. E. Gloriam, GPCRdb in 2021: Integrating GPCR sequence, structure and function. *Nucleic Acids Res.* **49**, D335–D343 (2021).
26. X. Lin, S. Jiang, Y. Wu, X. Wei, G. W. Han, L. Wu, J. Liu, B. Chen, Z. Zhang, S. Zhao, V. Cherezov, F. Xu, The activation mechanism and antibody binding mode for orphan GPR20. *Cell Discov.* **9**, 23 (2023).
27. J. Duan, D. D. Shen, X. E. Zhou, P. Bi, Q. F. Liu, Y. X. Tan, Y. W. Zhuang, H. B. Zhang, P. Y. Xu, S. J. Huang, S. S. Ma, X. H. He, K. Melcher, Y. Zhang, H. E. Xu, Y. Jiang, Cryo-EM structure of an activated VIP1 receptor-G protein complex revealed by a NanoBiT tethering strategy. *Nat. Commun.* **11**, 4121 (2020).
28. Y. L. Liang, P. Zhao, C. Draper-Joyce, J. A. Baltos, A. Glukhova, T. T. Truong, L. T. May, A. Christopoulos, D. Wootten, P. M. Sexton, S. G. B. Furness, Dominant negative G proteins enhance formation and purification of agonist-GPCR-G protein complexes for structure determination. *ACS Pharmacol. Transl. Sci.* **1**, 12–20 (2018).
29. S. Maeda, A. Koehl, H. Matile, H. Hu, D. Hilger, G. F. X. Schertler, A. Manglik, G. Skiniotis, R. J. P. Dawson, B. K. Kobilka, Development of an antibody fragment that stabilizes GPCR/G-protein complexes. *Nat. Commun.* **9**, 3712 (2018).
30. M. M. Rosenkilde, T. W. Schwartz, GluVII:06—A highly conserved and selective anchor point for non-peptide ligands in chemokine receptors. *Curr. Top. Med. Chem.* **6**, 1319–1333 (2006).
31. Q. Tan, Y. Zhu, J. Li, Z. Chen, G. W. Han, I. Kufareva, T. Li, L. Ma, G. Fenalti, J. Li, W. Zhang, X. Xie, H. Yang, H. Jiang, V. Cherezov, H. Liu, R. C. Stevens, Q. Zhao, B. Wu, Structure of the CCR5 chemokine receptor-HIV entry inhibitor maraviroc complex. *Science* **341**, 1387–1390 (2013).
32. Y. Zheng, L. Qin, N. V. O. Zacarías, H. de Vries, G. W. Han, M. Gustavsson, M. Dabros, C. Zhao, R. J. Cherney, P. Carter, D. Stamos, R. Abagyan, V. Cherezov, R. C. Stevens, A. P. IJzerman, L. H. Heitman, A. Tebben, I. Kufareva, T. M. Handel, Structure of CC chemokine receptor 2 with orthosteric and allosteric antagonists. *Nature* **540**, 458–461 (2016).
33. P. Isaikina, C.-J. Tsai, N. Dietz, F. Pamula, A. Grahl, K. N. Goldie, R. Guixà-González, C. Branco, M. Paolini-Bertrand, N. Calo, F. Cerini, G. F. X. Schertler, O. Hartley, H. Stahlberg, T. Maier, X. Deupi, S. Grzesiek, Structural basis of the activation of the CC chemokine receptor 5 by a chemokine agonist. *Sci. Adv.* **7**, eabg8685 (2021).
34. S. Connolly, M. Skrinjar, A. Rosendahl, Orally bioavailable allosteric CCR8 antagonists inhibit dendritic cell, T cell and eosinophil migration. *Biochem. Pharmacol.* **83**, 778–787 (2012).
35. D. J. Wasilko, Z. L. Johnson, M. Ammirati, Y. Che, M. C. Griffor, S. Han, H. Wu, Structural basis for chemokine receptor CCR6 activation by the endogenous protein ligand CCL20. *Nat. Commun.* **11**, 3031 (2020).
36. P. Isaikina, C. J. Tsai, N. Dietz, F. Pamula, A. Grahl, K. N. Goldie, R. Guixà-González, C. Branco, M. Paolini-Bertrand, N. Calo, F. Cerini, G. F. X. Schertler, O. Hartley, H. Stahlberg, T. Maier, X. Deupi, S. Grzesiek, Structural basis of the activation of the CC chemokine receptor 5 by a chemokine agonist. *Sci. Adv.* **7**, eabg8685 (2021).
37. S. G. F. Rasmussen, B. T. De Vree, Y. Zou, A. C. Kruse, K. Y. Chung, T. S. Kobilka, F. S. Thian, P. S. Chae, E. Pardon, D. Calinski, J. M. Mathiesen, S. T. A. Shah, J. A. Lyons, M. Caffrey, S. H. Gellman, J. Steyaert, G. Skiniotis, W. I. Weis, R. K. Sunahara, B. K. Kobilka, Crystal structure of the β2 adrenergic receptor-Gs protein complex. *Nature* **477**, 549–555 (2011).
38. H. E. Kato, Y. Zhang, H. Hu, C. M. Suomivuori, F. M. N. Kadji, J. Aoki, K. Krishna Kumar, R. Fonseca, D. Hilger, W. Huang, N. R. Latorraca, A. Inoue, R. O. Dror, B. K. Kobilka, G. Skiniotis, Conformational transitions of a neurotensin receptor 1-G(i1) complex. *Nature* **572**, 80–85 (2019).
39. T. Flock, C. N. J. Ravarani, D. Sun, A. J. Venkatakrishnan, M. Kayikci, C. G. Tate, D. B. Veprintsev, M. M. Babu, Universal allosteric mechanism for Gα activation by GPCRs. *Nature* **524**, 173–179 (2015).

40. L. Qin, I. Kufareva, L. G. Holden, C. Wang, Y. Zheng, C. Zhao, G. Fenalti, H. Wu, G. W. Han, V. Cherezov, R. Abagyan, R. C. Stevens, T. M. Handel, Structural biology. Crystal structure of the chemokine receptor CXCR4 in complex with a viral chemokine. *Science* **347**, 1117–1122 (2015).
41. K. Jaeger, S. Bruenle, T. Weinert, W. Guba, J. Muehle, T. Miyazaki, M. Weber, A. Furrer, N. Haenggi, T. Tetaz, C. Y. Huang, D. Mattle, J. M. Vonach, A. Gast, A. Kuglstatter, M. G. Rudolph, P. Nogly, J. Benz, R. J. P. Dawson, J. Standfuss, Structural basis for allosteric ligand recognition in the human CC chemokine receptor 7. *Cell* **178**, 1222–1230.e10 (2019).
42. C. Oswald, M. Rappas, J. Kean, A. S. Doré, J. C. Errey, K. Bennett, F. Deflorian, J. A. Christopher, A. Jazayeri, J. S. Mason, M. Congreve, R. M. Cooke, F. H. Marshall, Intracellular allosteric antagonism of the CCR9 receptor. *Nature* **540**, 462–465 (2016).
43. A. S. Dixon, M. K. Schwinn, M. P. Hall, K. Zimmerman, P. Otto, T. H. Lubben, B. L. Butler, B. F. Binkowski, T. Machleidt, T. A. Kirkland, M. G. Wood, C. T. Eggers, L. P. Encell, K. V. Wood, NanoLuc complementation reporter optimized for accurate measurement of protein interactions in cells. *ACS Chem. Biol.* **11**, 400–408 (2016).
44. A. Punjani, J. L. Rubinstein, D. J. Fleet, M. A. Brubaker, cryoSPARC: Algorithms for rapid unsupervised cryo-EM structure determination. *Nat. Methods* **14**, 290–296 (2017).
45. R. Sanchez-Garcia, J. Gomez-Blanco, A. Cuervo, J. M. Carazo, C. O. S. Sorzano, J. Vargas, DeepEMhancer: A deep learning solution for cryo-EM volume post-processing. *Commun. Biol.* **4**, 874 (2021).
46. E. F. Pettersen, T. D. Goddard, C. C. Huang, G. S. Couch, D. M. Greenblatt, E. C. Meng, T. E. Ferrin, UCSF Chimera—A visualization system for exploratory research and analysis. *J. Comput. Chem.* **25**, 1605–1612 (2004).
47. P. Emsley, B. Lohkamp, W. G. Scott, K. Cowtan, Features and development of Coot. *Acta Crystallogr. D Biol. Crystallogr.* **66**, 486–501 (2010).
48. A. J. McCoy, R. W. Grosse-Kunstleve, P. D. Adams, M. D. Winn, L. C. Storoni, R. J. Read, Phaser crystallographic software. *J. Appl. Cryst.* **40**, 658–674 (2007).
49. V. B. Chen, W. B. Arendall III, J. J. Headd, D. A. Keedy, R. M. Immormino, G. J. Kapral, L. W. Murray, J. S. Richardson, D. C. Richardson, MolProbity: All-atom structure validation for macromolecular crystallography. *Acta Crystallogr. D Biol. Crystallogr.* **66**, 12–21 (2010).

Acknowledgments: We thank Q. Sun, D. Liu, L. Wang, and S. Zheng at the Bio-EM facility at ShanghaiTech University, as well as J. Liu, Q. Tan, Q. Shi, X. Liu, N. Chen, F. Li, F. Zhou, S. Hu, P. Si, and L. Zhang for their contributions in protein cloning, expression, and assay support. **Funding:** This work was supported by the Ministry of Science and Technology of China (2018YFA0507000 to F.X.), National Natural Science Foundation of China (32071194 to F.X.), Shanghai Science and Technology Plan (21DZ2260400 to F.X.), Shanghai Ninth People's Hospital, and Shanghai JiaoTong University School of Medicine–Shanghai University of Science and Technology Cross-funded Collaborative Program (JYJC202233 to F.X.). **Author contributions:** Writing—original draft: F.X., S.J., and X.L. Conceptualization: F.X. Investigation: F.X. and S.J. Writing—review and editing: F.X. Methodology: F.X., S.J., X.L., L. Wu, L. Wang, Y.W., and Z.X. Resources: F.X. Funding acquisition: F.X. Data curation: F.X., S.J., and L. Wang. Validation: F.X. and S.J. Supervision: F.X. Project administration: F.X. Visualization: F.X. and S.J. Formal analysis: S.J., X.L., L. Wu, and Y.W. **Competing interests:** The authors declare that they have no competing interests. **Data and materials availability:** All data needed to evaluate the conclusions in the paper are present in the paper and/or the Supplementary Materials. Cryo-EM maps of the apo-CCR8-G_i, ZK 756326–CCR8–G_i, and LMD-009–CCR8–G_i complexes have been deposited in the Electron Microscopy Data Bank under accession codes EMD-37209, EMD-37208, and EMD-37207, respectively. Atomic coordinates and structure factors for the reported cryo-EM structures have been deposited with the PDB under the access codes 8KFZ, 8KFY, and 8KFX.

Submitted 17 July 2023
Accepted 3 January 2024
Published 2 February 2024
10.1126/sciadv.adj7500